Spectroscopic evaluation of charge-transfer doping and strain in graphene/MoS$_2$ heterostructures

Rahul Rao,[1,2,*] Ahmad E. Islam,[1,2] Simranjeet Singh,[3] Rajiv Berry,[1] Roland K. Kawakami,[4]
Benji Maruyama,[1] and Jyoti Katoch[3,†]

[1]*Materials and Manufacturing Directorate, Air Force Research Laboratory, Wright Patterson AFB, Ohio 45433, USA*
[2]*UES Inc., Dayton, Ohio 45425, USA*
[3]*Department of Physics, Carnegie Mellon University, Pittsburgh, Pennsylvania 15213, USA*
[4]*Department of Physics, The Ohio State University, Columbus, Ohio 43210, USA*

It is important to study the van der Waals interface in emerging vertical heterostructures based on layered two-dimensional (2D) materials. Being atomically thin, 2D materials are susceptible to significant strains as well as charge-transfer doping across the interfaces. Here we use Raman and photoluminescence spectroscopy to study the interface between monolayer graphene/MoS$_2$ heterostructures prepared by mechanical exfoliation and layer-by-layer transfer. By using correlation analysis between the Raman modes of graphene and MoS$_2$, we show that both layers are subjected to compressive strain and charge-transfer doping following mechanical exfoliation and thermal annealing. Furthermore, we show that both strain and carrier concentration can be modulated in the heterostructures with additional thermal annealing. Our study highlights the importance of considering both mechanical and electronic coupling when characterizing the interface in van der Waals heterostructures, and it demonstrates a method to tune their electromechanical properties.

I. INTRODUCTION

The advent of two-dimensional (2D) layered materials beyond graphene has initiated a new field of research in vertical and lateral heterostructures wherein the stacking between the layers occurs through the weakly attractive van der Waals force. This allows the creation of a seemingly limitless number of artificial architectures where the properties of each layer can be combined toward unique applications [1] in electronics [2], optoelectronics [3], and photovoltaics [4]. Among the layered 2D materials, graphene and the semiconducting transition-metal dichalcogenide MoS$_2$ are arguably the most heavily studied. Graphene is an atomically thin semimetal, while monolayer MoS$_2$ is a direct-band-gap semiconductor with an optical gap of ~1.8 eV. The interaction between graphene and MoS$_2$ in vertical heterostructures has been reported in several publications in the literature, with some results in conflict with each other. The transfer of both holes [5] and electrons [6] from MoS$_2$ to graphene has been reported, as well as reports of no charge-transfer at all between the two [7,8]. Here we show that the discrepancies between the reported results may be explained by considering strain.

Being atomically thin, 2D layers can be subjected to significant in-plane and out-of-plane strains. The lattice deformation caused by such strains could adversely affect the thermal [9] and electrical [10,11] conductivities of the heterostructure, although studies have shown that their optoelectronic properties can be manipulated by strain engineering [12]. Both compressive and tensile strains have been found in graphene and MoS$_2$ within a vertical heterostructure [10,13,14]. These strains likely originate during the mechanical transfer process,

although thermal annealing and substrate interactions could impose additional strains on the 2D layers.

Raman and photoluminescence (PL) spectroscopy are arguably the most useful methods to study both strain and doping in graphene and MoS$_2$. The frequencies of the two major Raman peaks in graphene (G and G' peaks) and in MoS$_2$ (E' and A' peaks) are influenced by charge-transfer doping and strain, and correlation analysis between the two modes offers a way to decouple their effects [15–22]. That is, by plotting the frequencies of the G' (E') band against the G (A') band in graphene (MoS$_2$), one can establish the extent of strain versus doping in each layer. In addition to Raman peaks, monolayer MoS$_2$ exhibits strain- and doping-dependent PL emission, offering an additional means to study the interaction between graphene and MoS$_2$.

Here, by performing correlation analysis using Raman and PL spectroscopy, we show how strain and doping both affect graphene and MoS$_2$ when graphene is placed onto MoS$_2$ in a vertical heterostructure. We map two monolayer graphene/MoS$_2$ heterostructures and observe the following upon photoexcitation: (i) electrons are transferred from MoS$_2$ to graphene, and (ii) both graphene and MoS$_2$ are strained compressively. The degree of strain and doping varies between the two heterostructures and we show how a simple thermal annealing treatment can modulate both strain and doping. Our results highlight the effects of mechanical and electronic coupling between atomically thin layers subjected to van der Waals interactions, and at the same time we demonstrate a practical method to tune the electronic and mechanical properties of van der Waals heterostructures.

II. SAMPLE PREPARATION

Bulk graphite and MoS$_2$ were mechanically exfoliated with tape to obtain monolayer graphene and MoS$_2$ onto

*rahul.rao.1.ctr@us.af.mil
†jkatoch@andrew.cmu.edu

separate SiO$_2$/Si substrates. For fabricating graphene/MoS$_2$ heterostructures, a polymer-based pick-up technique was utilized for the transfer process [23,24]. First, a small piece of polydimethylsiloxane (PDMS) stamp was attached on a glass slide. Separately, a polycarbonate (PC) film was prepared on another glass slide by putting a few drops of PC solution and spreading it across the slide. Then PC film was peeled off from the glass slide and attached onto the PDMS stamp. This PC/PDMS glass slide was then used to first pick up graphene from SiO$_2$ substrate. For this, a PC/PDMS glass slide was brought in contact with the graphene and then the polymer was softened by heating it to 90 °C. Subsequently, the polymer was cooled to room temperature to pick up graphene from the SiO$_2$ substrate. Next, this PC film carrying graphene was aligned with the monolayer MoS$_2$ on SiO$_2$ substrate under an optical microscope and then PC film melted onto MoS$_2$ by heating it up to 150 °C. Finally, the PC polymer was removed by rinsing the substrate in chloroform for about 10–15 min to obtain a graphene/MoS$_2$ heterostructure.

III. RESULTS

Both monolayer graphene and MoS$_2$ are prepared on Si/SiO$_2$ substrates by mechanical exfoliation, followed by transfer of the graphene on to MoS$_2$ (see details in Sec. II). After transfer, the samples first undergo annealing under vacuum (370 °C at 10^{-5} torr for 3 h) and then under a mixture of Ar and H$_2$ (350 °C for 3 h) to remove trapped residues and to improve the coupling between the two layers. Figure 1(a) shows an optical microscope image collected from a graphene/MoS$_2$ heterostructure (Het-1). The graphene layer can be identified by the slightly darker contrast compared to the underlying SiO$_2$ substrate; the dashed outline serves as a guide. Figure 1(b) shows a two-dimensional (2D) Raman intensity map of the first order G peak in graphene, corresponding to in-plane vibrations of the sp^2 bonded carbon atoms. All spectra are collected with 514.5 nm laser excitation in a Renishaw Raman microscope with a 100× objective lens (producing a 600 nm spot size). The laser power is kept under 70 μW to minimize sample heating. The intensity map of the E' peak in MoS$_2$ is shown in Fig. 1(c). Similar to the graphene G peak, the E' peak in MoS$_2$ corresponds to in-plane vibrations. A comparison between Figs. 1(b) and 1(c) shows the presence of graphene and MoS$_2$ on SiO$_2$ outside the heterostructure [also indicated by the arrows in the optical microscope image in Fig. 1(a) and hereafter referred to as bare graphene and MoS$_2$]. This allows us to compare between their spectra on the bare substrate and in the vertical heterostructure. The other prominent peak in the Raman spectrum of graphene is the G' peak, which arises from scattering of photoexcited electrons by two transverse optical phonons. The G' peak is typically much more intense than the G peak in the Raman spectrum from monolayer graphene, as seen in the intensity ratio ($I_{G'}/I_G$) map in Fig. 1(d). $I_{G'}/I_G$ decreases by a factor of 2–3 in the heterostructure and is attributed to charge-transfer doping [25].

Both graphene and MoS$_2$ Raman peaks exhibit significant changes in their frequencies and linewidths inside the heterostructure. We attribute these changes to strain and charge-transfer doping, as explained further below. The graphene

G peak frequency (ω_G) redshifts by 8–10 cm^{-1} in the heterostructure, as seen in the 2D frequency map in Fig. 1(e). On the other hand, the G' peak blueshifts ($\omega_{G'}$) by 5–10 cm^{-1} between SiO$_2$ and the heterostructure [Fig. 1(f)]. Both graphene peaks also exhibit significant broadening in the heterostructure compared to SiO$_2$, with the G peak broadening (Γ_G) from ~10 cm^{-1} in bare graphene to ~25 cm^{-1} in the heterostructure [Fig. 1(g)]. The linewidth of the G' peak $\Gamma_{G'}$, which is often correlated to graphene quality, is ~25 cm^{-1} in bare graphene and broadens to ~45 cm^{-1} in the heterostructure. The Raman peaks of MoS$_2$ also undergo changes in intensity and frequency. Both E' [Fig. 1(i)] and A' [Fig. 1(j)] peaks blueshift in frequency by an average of 2 cm^{-1} in the heterostructure. In addition, both peaks narrow by 2–3 cm^{-1} in the heterostructure compared to bare MoS$_2$ [Fig. 1(k) shows a 2D linewidth map of the E' peak].

Taken together, the maps in Figs. 1(b)–1(k) show that the Raman peaks of both graphene and MoS$_2$ shift in frequency when the two layers are in contact with each other. As-deposited graphene and MoS$_2$ on SiO$_2$ substrates are known to be p-type and n-type doped, respectively [25–28]. This charge state comes from interaction with the SiO$_2$ substrate and the ambient environment [26,27], and in the case of MoS$_2$ the additional electron density could also originate from sulfur vacancies [28,29]. Thus, when graphene is placed onto MoS$_2$, we expect MoS$_2$ to donate electrons to graphene, and that is what we infer from the data shown in Fig. 1. Both the G and G' peaks in bare graphene are blueshifted in frequency (p-doped or hole-doped) compared to the frequency of pristine undoped graphene [30], while they are redshifted within the heterostructure, suggestive of electron transfer from the underlying MoS$_2$. Similarly, the blueshift of the MoS$_2$ Raman peaks indicates electron transfer to the graphene [31].

However, the linewidths of the graphene and MoS$_2$ Raman peaks do not follow the trends established for charge-transfer doping. We observe broadening of the G peak by as much as 15 cm^{-1}, whereas it sharpens for both electron and hole doping due to the strong electron-phonon coupling of the G peak phonons. This coupling reduces the number of decay channels due to Pauli blocking [30,32]. Considering that our graphene on SiO$_2$ is already p-doped, a slight peak narrowing is expected upon electron transfer from MoS$_2$ to graphene. However, the observation of significant broadening hints at a different mechanism, which we attribute to strain. In the case of MoS$_2$, upon hole-doping the Raman peaks have been observed to sharpen [6,33], in agreement with our observation of peak linewidth narrowing in the heterostructure [Fig. 1(k)].

IV. DISCUSSION

The Raman frequencies (ω) are related to lattice strain (ε) by the Grüneisen parameter (γ), according to the following equation:

$$\Delta\omega = -2\gamma_i\omega_i^0\varepsilon_i, \tag{1}$$

where γ_i is the Grüneisen parameter corresponding to the frequency of peak i (ω_i), and ω_i^0 is the frequency corresponding to zero strain. The Grüneisen parameter has been experimentally determined for both graphene [21,34–37] and MoS$_2$ [38,39]. Average room-temperature γ values for
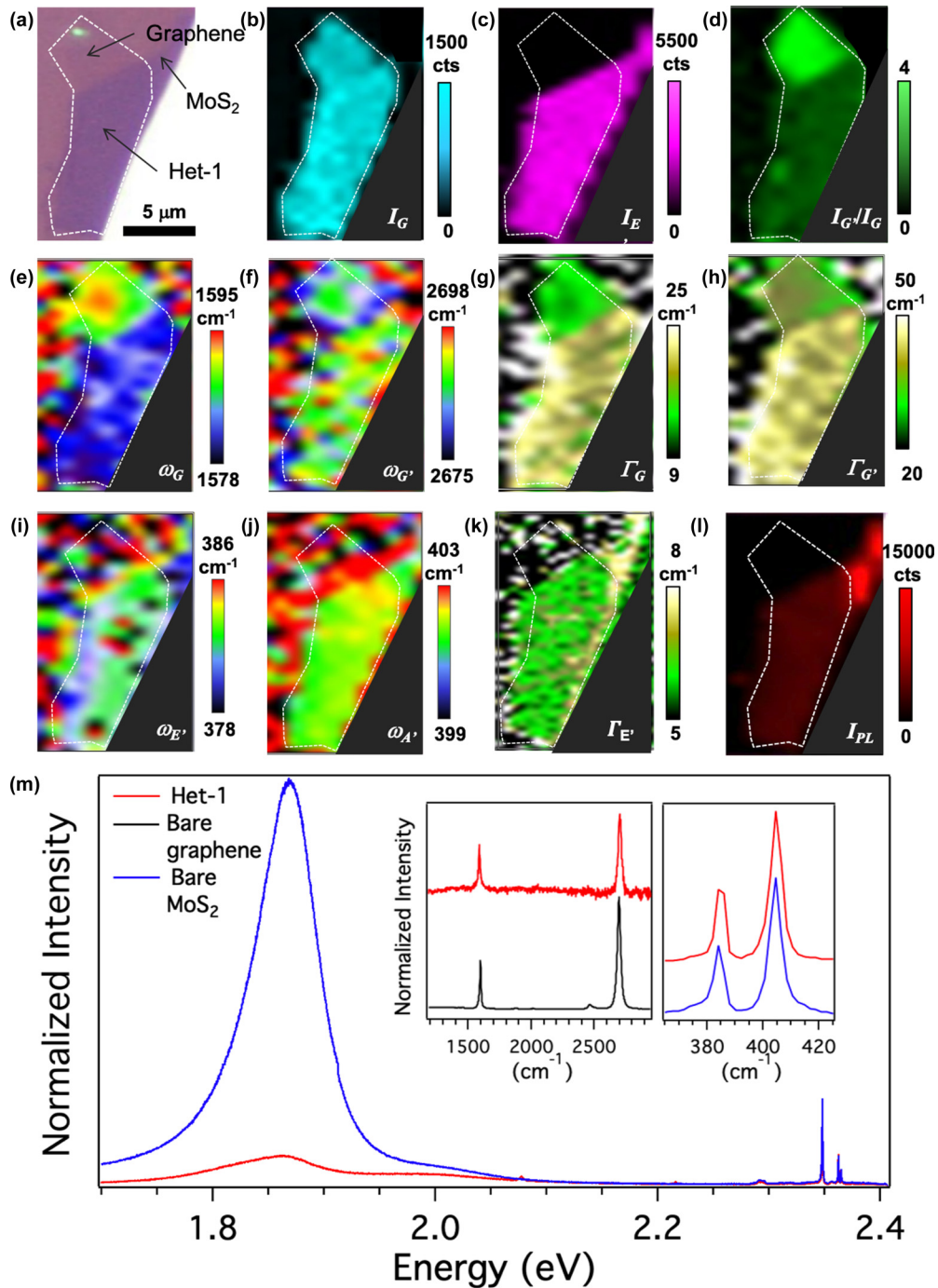
FIG. 1. Optical characterization of a graphene/MoS$_2$ heterostructure on SiO$_2$ (Het-1). (a) Optical microscope image of Het-1. The top layer (monolayer graphene) is shown by the dashed outline. 2D Raman intensity maps are shown for the (b) graphene G peak and (c) MoS$_2$ E' peaks. (d) Intensity ratio of the graphene G' and G peaks showing a suppression of the G' peak intensity within the heterostructure. (e), (f) Maps showing frequencies of the graphene G and G' peaks, respectively. (g), (h) Maps showing linewidths (FWHM) of the graphene G and G' peaks, respectively. (i), (j) Maps showing frequencies of the MoS$_2$ E' and A' peaks, respectively. (k) Map showing linewidths (FWHM) of the MoS$_2$ E' peak. (l) Map of the PL emission intensity from the MoS$_2$. (m) Representative PL emission spectra (normalized to the SiO$_2$ substrate Raman peak intensity) from MoS$_2$ on SiO$_2$ (top trace) and the graphene/MoS$_2$ heterostructure (bottom trace). The left inset shows the Raman peaks from the bare graphene (bottom trace) and graphene in Het-1 (top trace). The right inset shows the Raman peaks from the bare MoS$_2$ (bottom trace) and MoS$_2$ within Het-1 (top trace).

uniaxial strain from the literature are 1.9, 2.6, 0.86, and 0.15 for the G, G', E', and A' peaks, respectively. Furthermore, the doping dependence of the graphene [30] and MoS$_2$ [31] peak frequencies has been experimentally measured and found to

be quasilinear for electron and hole doping in MoS$_2$ and for hole doping in graphene [30,31], while it is nonlinear for electron doping in graphene [30]. However, here we neglect electron doping in graphene because of many studies that have

shown graphene to be *p*-doped on SiO$_2$ substrates [40,41]. Assuming a linear relationship, we have the relation between the peak frequency and carrier concentration as follows:

$$\omega_i = k_n(i)n. \tag{2}$$

Here n is the carrier concentration and $k_n(i) = -0.33 \times 10^{13}$, -2.22×10^{13}, -9.6×10^{13}, and -1×10^{13} for $I = E'$, A', G, and G' peaks, respectively. The constants $k_n(i)$ have been determined empirically in [30,31]. Since the peak frequencies depend on both strain and carrier concentration, we combine Eqs. (1) and (2) to obtain a pair of equations:

$$\Delta\omega_1 = -2\gamma_1\omega_1^0\varepsilon + k_n(1)n, \tag{3}$$

$$\Delta\omega_2 = -2\gamma_2\omega_2^0\varepsilon + k_n(2)n. \tag{4}$$

Here the subscripts 1 and 2 refer to the pair of peaks G and G' for graphene, and E' and A' for MoS$_2$, respectively. Equations (3) and (4) can be rearranged and expressed in terms of ε and n as follows:

$$\varepsilon = \frac{k_n(1)\Delta\omega_2 - k_n(2)\Delta\omega_1}{2\gamma_1\omega_1^0 k_n(2) - 2\gamma_2\omega_2^0 k_n(1)}, \tag{5}$$

$$n = \frac{\gamma_1\omega_1^0\Delta\omega_2 - \gamma_2\omega_2^0\Delta\omega_1}{\gamma_1\omega_1^0 k_n(2) - \gamma_2\omega_2^0 k_n(1)}. \tag{6}$$

Equations (5) and (6) enable the calculation of Raman peak frequencies for constant strain and carrier concentration. To perform this calculation, one must first establish the Raman peak frequencies for unstrained and undoped graphene and MoS$_2$. For this we choose the Raman frequencies from suspended graphene [19,42–44] and MoS$_2$ [45–47], which can be considered as their pristine unperturbed state. A plot between the calculated graphene G' and G peak frequencies and between the MoS$_2$ E' and A' peaks can then be drawn with superimposed constant strain (ε) and constant carrier concentration (n) axes as shown in Fig. 2. The calculated constant ε and constant n axes are drawn on the ε-n plot for increments of 0.1% and 0.5×10^{13} cm^{-2}, respectively, with positive (negative) strain values corresponding to tension (compression). The straight lines denote zero strain and doping, and the green square data point corresponds to the Raman peak frequency for suspended graphene and MoS$_2$. We now plot the experimentally measured Raman peak frequencies (Fig. 1 of this paper and Fig. S1 of the Supplemental Material [58]) from graphene and MoS$_2$ from both the vertical heterostructures on the ε-n plot. (Fig. 3).

Comparing the data between bare graphene (blue circles for Het-1 and blue triangles for Het-2) and graphene on MoS$_2$ (red circles for Het-1 and red triangles for Het-2) points in Fig. 3(a), one immediately sees that they are different and shifted from each other. The bare graphene in both Het-1 and Het-2 is *p*-doped, with an average hole concentration of $\sim$1.4 $\times$ 10^{13} cm^{-2}. In addition, bare graphene is also under tensile strain (up to 0.3%), with the average strain slightly higher in Het-2 than Het-1. For the graphene in the heterostructure, the G and G' peaks are redshifted and blueshifted in frequency, respectively, implying a reduction in hole concentration from $\sim$1.4 $\times$ 10^{13} cm^{-2} to an average
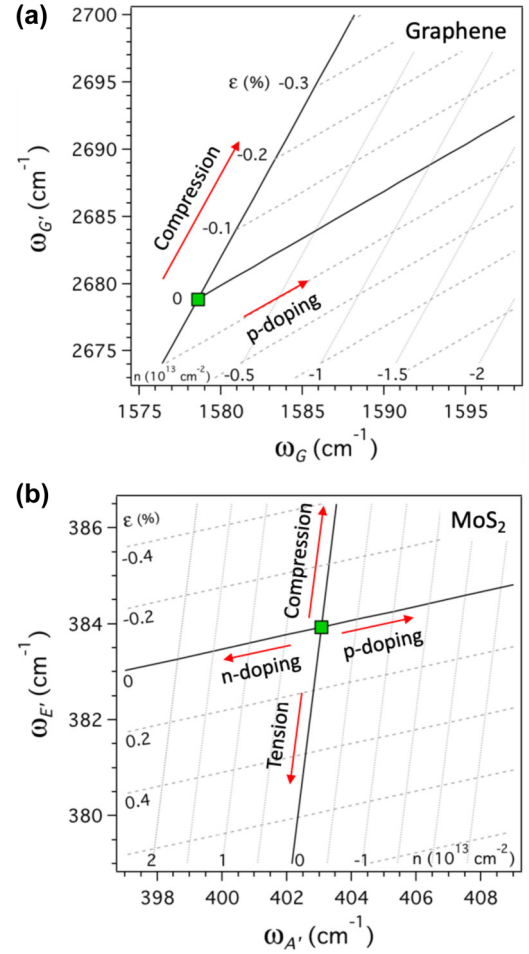

FIG. 2. ε-n plots for (a) graphene and (b) MoS$_2$ calculated using Eqs. (5) and (6) for various strain and carrier concentration values. The green square data points correspond to undoped and unstrained graphene and MoS$_2$, which we assume to be the Raman peak frequencies from suspended layers.

of 0.4×10^{13} cm^{-2}. Furthermore, the tensile strain in the bare graphene converts to compressive strain in both heterostructures. The black arrow in Fig. 3(a) indicates the overall shift of the Raman peaks from bare graphene to graphene in the heterostructures.

Figure 3(b) shows the ε-n plot with the MoS$_2$ E' and A' Raman peaks from Het-1 and Het-2. Unlike graphene, where the peak frequencies in both heterostructures are similar, bare MoS$_2$ in the two heterostructures exhibits differences in charge and strain states. However, within both heterostructures the MoS$_2$ donates electrons to graphene and undergoes compression to varying degrees. Bare MoS$_2$ in Het-1 [blue circles in Fig. 3(b)] is *n*-doped with an average electron density of $\sim$1 $\times$ 10^{13} cm^{-2} and is under tensile strain (average $\sim$0.38%). It undergoes compression (strain relief) in the heterostructure to an almost unstrained state. The MoS$_2$ in Het-1 donates electrons to graphene, and its electron density is lowered from $\sim$1 $\times$ 10^{13} in bare MoS$_2$ to $\sim$0.5 $\times$ 10^{13} cm^{-2} in the heterostructure. Bare MoS$_2$ in Het-2 is slightly *p*-doped and under tension and undergoes slight compression and *p*-doping within the heterostructure.
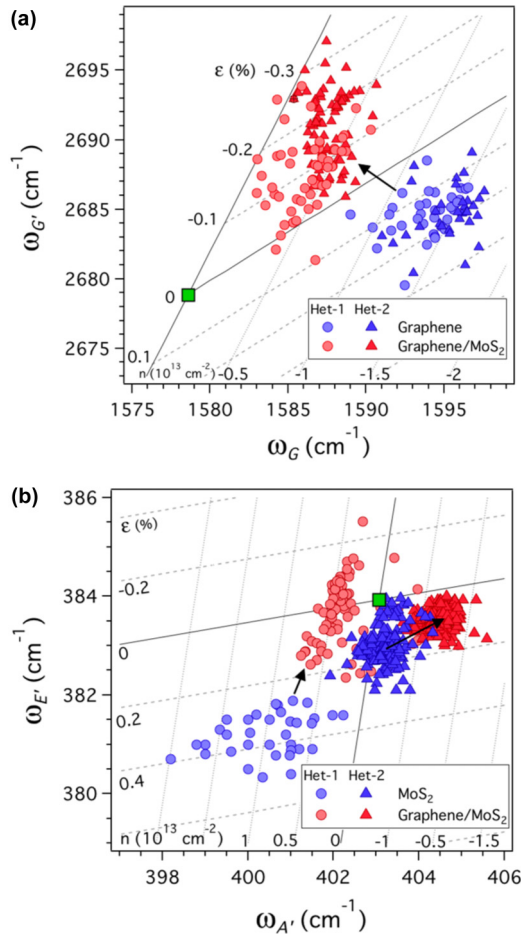
FIG. 3. Strain-doping (ε-n) plots for two different graphene/MoS_2 heterostructures (Het-1, circles and Het-2, triangles) obtained by plotting frequencies of the (a) G' vs G peak for graphene on SiO_2 and graphene in the heterostructure, and (b) A' vs E' peak for MoS_2 on SiO_2 and MoS_2 in the heterostructure. The green data points in (a) and (b) correspond to Raman frequencies of suspended graphene and MoS_2, respectively. The shift in frequencies from bare SiO_2 to the heterostructure are indicated by the arrows.

The Raman frequencies, strains, and carrier concentrations in bare graphene and MoS_2 and within the two heterostructures are tabulated in Table I. Graphene in both the heterostructures behaves in a similar fashion with respect to strain and charge transfer (undergoes compression and gains electrons from MoS_2), and MoS_2 loses electrons to graphene while also undergoing compression in the heterostructure. While the graphene Raman peak frequencies are very similar in the two heterostructures, the MoS_2 in Het-2 is influenced more by doping [data points shift toward the right in Fig. 3(b)] than in Het-1 where the influence of strain is greater than doping [data points shift upward in Fig. 3(b)].

Although it is not surprising to find that the electron-rich MoS_2 donates electrons to electron-poor graphene, the observation of compressive strain in both layers (up to 0.3%) in two different heterostructures is noteworthy. Graphene has a negative coefficient of thermal expansion (CTE) of $\sim-8 \times 10^{-6} K^{-1}$ at 300 K [48,49], while the CTE for MoS_2 is positive ($\sim6 \times 10^{-6} K^{-1}$ at 300 K) [49]. The CTEs of both

graphene and MoS_2 are an order of magnitude larger than that of SiO_2 ($\sim0.6 \times 10^{-6} K^{-1}$) [50]. Since our samples undergo thermal annealing (350 °C) after mechanical exfoliation, one could expect the emergence of strain in the graphene and MoS_2 due to the differences between their CTEs and the much smaller CTE of the SiO_2 substrate, as well as the differences between the lattice constants of graphene (2.40 Å) and MoS_2 (3.12 Å). Indeed, large tensile and compressive strains (up to 0.7%) have been observed in bare MoS_2 and graphene on substrates upon heating and cooling [20,21,51]. Note that compressive and tensile strains are also observed in as-transferred graphene and MoS_2 without any thermal annealing [15,18]. Our observed strain values in bare graphene and MoS_2 are within the range of strains published in the literature, and also match the calculated values ($\sim0.1\%$) for cooling from 350 °C to room temperature.

It is important to reiterate that the strains and carrier concentrations in our graphene/MoS_2 heterostructures are calculated based on the Raman frequencies of the respective suspended layers, which we assume to be unstrained and undoped. The absolute values of the initial charge state and strain cannot be known unless they are measured independently. However, we can still compare the relative increases or decreases of Raman frequencies in the heterostructures compared to bare SiO_2, and therefore our observation of electron transfer from MoS_2 to graphene and compressive strain in the heterostructures is valid. While these observations suggest a universal trend, the magnitudes of charge transfer and strain are evidently different between Het-1 and Het-2.

So far, we have discussed the differences in Raman peak frequencies inside and outside the heterostructure. For MoS_2 we can also analyze the PL emission intensities and energies. As shown in Figs. 1(l) and 1(m), the PL emission gets quenched drastically by over 90% from bare MoS_2 to the heterostructure. Quenching of the MoS_2 PL intensity has been observed before in graphene/MoS_2 heterostructures and is generally attributed to the coupling between the two layers [3,52–54]. The PL emission in MoS_2 occurs from a recombination of photoexcited excitons corresponding to an optical band gap of ~1.83 eV [55,56]. The PL emission band typically also contains a second peak at a lower energy, corresponding to a recombination of trions (excitons formed by two electrons/one hole or two holes/one electron) [57]. As-deposited MoS_2 on SiO_2 is typically electron-rich (n-type), resulting in an abundance of negative trions, hence one expects to see a higher trion peak intensity in the PL emission. Moreover, in general the PL emission energy redshifts (blueshifts) with hole (electron) doping. But the electronic structure of a material is also influenced by strain. The band gap of monolayer MoS_2 depends approximately linearly on the applied strain at rates ranging from -25 to -45 meV/% [10]. Tensile (compressive) strain typically results in a redshift (blueshift) of the emission energy, along with broadening of the PL emission peaks.

In Het-1 we observe a blueshift of the emission by up to 20 meV as shown in the 2D PL emission map in Fig. 4(a). By extracting a couple of representative spectra from the 2D PL emission map [Fig. 4(a)] and by performing Lorentzian line-shape analysis, we can see blueshifts in both the A^- (trion) and A (neutral exciton) peak energies [Fig. 4(b)], suggesting that

TABLE I. Range of Raman peak frequencies and their average values (in bold, within parentheses) measured from bare graphene (top) and MoS$_2$ (bottom) and within the two heterostructures. Also included are the estimated ranges of strain and carrier concentration. Positive (negative) numbers correspond to tension and electron (compression and hole) doping.

Graphene					
		G (cm^{-1})	G' (cm^{-1})	Strain (%)	Carrier concentration (× 10^{13} cm^{-2})
Het-1	Bare	1587 to 1596 (***1594.3***)	2680 to 2688 (***2684.7***)	0.03 to 0.28 (***0.12***)	-0.7 to -1.5 (***-1.3***)
Het-1	Heterostructure	1583 to 1590 (***1586.3***)	2686 to 2694 (***2687.7***)	0.1 to -0.28 (***-0.15***)	0 to -0.5 (***-0.4***)
Het-2	Bare	1591 to 1597 (***1595.3***)	2683 to 2686 (***2684.7***)	0.02 to 0.3 (***0.15***)	-1.1 to -1.7 (***-1.5***)
Het-2	Heterostructure	1585 to 1590 (***1587.7***)	2686 to 2695 (***2691***)	0 to 0.33 (***-0.18***)	0 to -0.6 (***-0.3***)
MoS$_2$					
		E' (cm^{-1})	A' (cm^{-1})	Strain (%)	Carrier concentration (× 10^{13} cm^{-2})
Het-1	Bare	380 to 381.5 (***381***)	398 to 402 (***400***)	0.26 to 0.5 (***0.4***)	0 to 2 (***1***)
Het-1	Heterostructure	382 to 385 (***383***)	400.5 to 402 (***401.5***)	0.2 to -0.2 (***0***)	-1 to 0.5 (***0.4***)
Het-2	Bare	381.5 to 383.5 (***382.5***)	402 to 404 (***401***)	0 to 0.3 (***0.15***)	0.4 to -1 (***0.3***)
Het-2	Heterostructure	382.5 to 383.5 (***383***)	402.5 to 405 (***404***)	0 to 0.2 (***0.1***)	-0.5 to -1.2 (***0.1***)

(Column annotations: Graphene Strain → Compression; Graphene Carrier concentration → Gains e⁻. MoS$_2$ Strain → Compression; MoS$_2$ Carrier concentration → Loses e⁻.)

the PL from the MoS$_2$ in Het-1 is influenced more by strain than by doping. Furthermore, the magnitude of the blueshift (ranging from 10 to 20 meV) corresponds to strains ranging from 0.2% to 0.5%; this matches very well with the observed Raman frequencies. In contrast, the Raman spectra from the MoS$_2$ in Het-2 show that it is influenced more by doping than by strain [Fig. 3(b)]. This can also be seen in the PL emission maps in Fig. 4(c), where we plot the 2D emission maps for both A and B excitons. Note that the broad PL emission peaks in Het-2 make it difficult to deconvolve the trion and neutral exciton peaks, hence we fit it to a single Lorentzian peak labeled A. Fits to representative spectra from Het-2 reveal a slight redshift, which we attribute to hole doping.

To see if it is possible to modulate the carrier concentration or the strain in the heterostructures, we investigate the effect of additional thermal annealing. Figure 5 shows the Raman peak

frequencies of graphene and MoS$_2$ in Het-1 [Figs. 5(a) and 5(b)] and Het-2 [Figs. 5(c) and 5(d)] after thermal annealing at 350 °C for 30 min under flowing argon at atmospheric pressure. The Raman peak frequencies corresponding to the unannealed (same as in Fig. 3) and annealed states are shown as light and dark data points, respectively. In both heterostructures we see that bare graphene becomes more p-doped, with similar increases in hole concentration (from ∼1.4 to ∼1.6 × 10^{13} cm^{-2} on average) upon thermal annealing [Figs. 5(a) and 5(c)]. Although both heterostructures are annealed under flowing argon gas, the process is performed at atmospheric pressure and the increase in hole concentration can be attributed to doping from residual oxygen in the chamber [16,18]. Interestingly, however, annealing affects the strain differently in bare graphene. After the additional annealing, the tensile strain in bare graphene in Het-1 increases slightly,
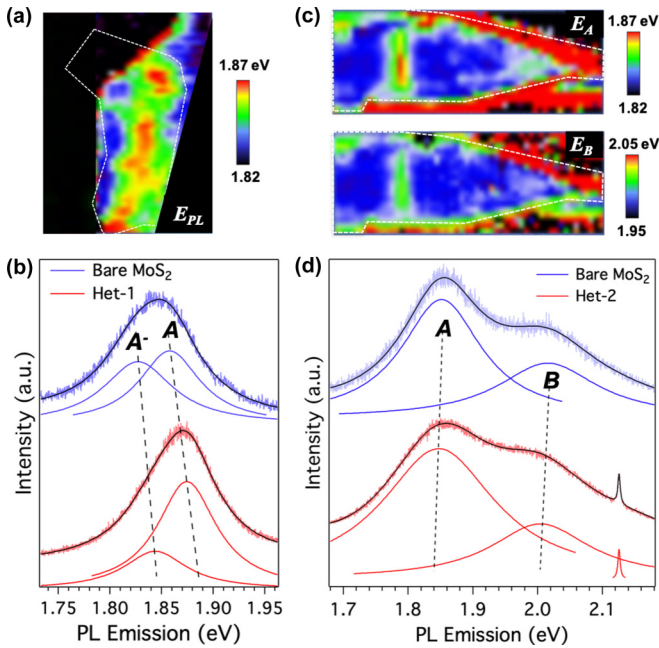
FIG. 4. 2D PL emission maps and representative Raman spectra from (a) Het-1 and (b) Het-2. The overall blueshift and redshifts observed in Het-1 and Het-2 indicate greater influences from compressive strain and doping, respectively.

while it decreases to an almost unstrained state in Het-2. Within the heterostructure, the additional annealing causes the graphene to undergo compressive strain and become less hole-doped by accepting electrons from the underlying MoS_2 layer. The overall direction of change in graphene peak frequencies is the same as that observed prior to thermal annealing (data points move to the left and upward on the ε-n plot, i.e., compression and reduction in hole concentration between bare graphene and graphene in the heterostructure). But the magnitude of strain is different in the two heterostructures—graphene in Het-2 undergoes much more compression (up to 0.5%) after the additional annealing compared to Het-1.

In the case of MoS_2, thermal annealing causes both heterostructures to behave in a similar fashion, with bare MoS_2 undergoing compression and p-doping. However, the additional annealing affects bare MoS_2 in Het-1 much more than in Het-2. It undergoes significant p-doping (up to 2×10^{13} cm^{-2}) and compression (0.4% on average) to an almost unstrained state. Within the heterostructure the MoS_2 in Het-1 undergoes further compressive strain ($\sim$0.1% on average) and hole-doping. The annealing does not appear to affect the MoS_2 in Het-2 as much as in Het-1, although the general trend is the same (p-doping and compression). After thermal annealing the PL emission from MoS_2 in both heterostructures remains blueshifted compared to bare MoS_2.
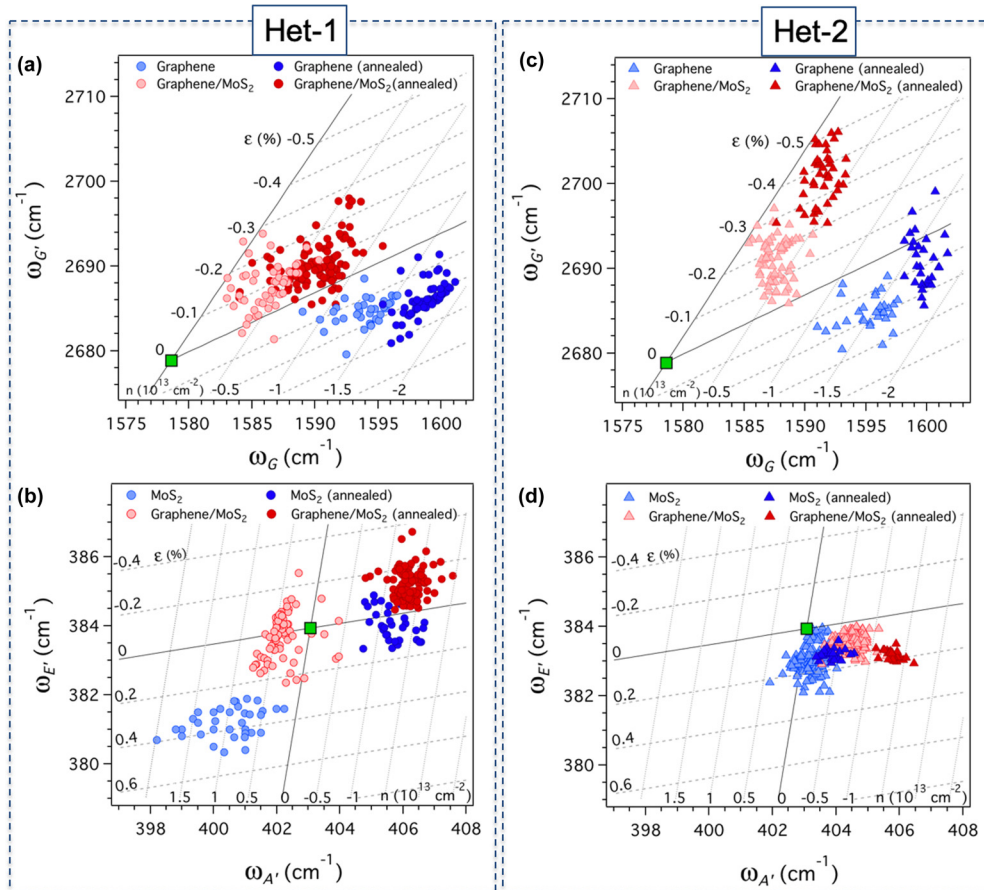

FIG. 5. Raman peak frequencies from Het-1 (a), (b) and Het-2 (c), (d) after thermal annealing at 350 °C under atmospheric pressure argon. The lighter (darker) data points correspond to before (after) annealing. The ε-n plots are drawn on the same scale to show how thermal annealing affects the strain and carrier concentration in graphene/MoS_2 heterostructures prepared under similar conditions.

The ε-n plots in Fig. 5 demonstrate an approach to modulate the strain and carrier concentration in graphene/MoS$_2$ heterostructures through thermal annealing. While we have only shown the effects of thermal annealing under argon at atmospheric pressure, other forms of annealing, for example in vacuum, photonic annealing, or exposure to other environments, could be employed to tune the strain and carrier concentration in graphene/MoS$_2$ and other 2D heterostructures. Figure 5 also draws attention to an important issue regarding sample preparation, namely reproducibility. Our results show that samples that have been prepared under similar conditions (mechanical exfoliation followed by transfer) behave quite differently depending upon thermal annealing. The reason for this difference is unclear and requires further experimental and theoretical investigations.

Finally, the variations in the carrier concentrations and strain states in the heterostructures suggest that the discrepancies reported in the literature could be attributed to different charge and strain states of graphene and MoS$_2$ after sample preparation. Moreover, the clear differences between two heterostructures that were prepared by the same method highlight inherent variabilities in the mechanical transfer processes and point to the need for a fast and convenient method to characterize these differences. Our usage of ε-n plots shows that it is important to concurrently measure strain and doping, both of which can easily affect atomically thin materials. Although here we considered uniaxial strains in the 2D layers, we cannot exclude biaxial strain, and further experimental and theoretical analysis could provide more insights. The van der Waals interface between 2D materials is highly sensitive to the processing conditions, and care must be taken during sample preparation and characterization. The method described herein can also be extended to other materials toward strain engineering and tuning the carrier concentration in 2D heterostructures.

V. CONCLUSIONS

We have studied coupling-induced charge-transfer doping and strain in two graphene/MoS$_2$ heterostructures using Raman and PL spectroscopy. By using correlation analysis between the G' and G peaks in graphene and between the E' and A' Raman peaks in MoS$_2$, we show that graphene (MoS$_2$) is p-doped (n-doped) on SiO$_2$ and that there is a transfer of electrons from MoS$_2$ to graphene. Moreover, we find bare graphene and MoS$_2$ on SiO$_2$ to be affected by varying degrees of strains, likely induced during the transfer process. Within the heterostructure, we find both graphene and MoS$_2$ to undergo compressive strain. Interestingly, both charge concentration and strain can be tuned to a certain degree with thermal annealing. Our study shows that it is important to consider both mechanical and electronic coupling when characterizing van der Waals interfaces in 2D heterostructures, and at the same time it demonstrates a way to modulate strain and carrier concentration through annealing.

[1] A. K. Geim and I. V. Grigorieva, Nature (London) **499**, 419 (2013).

[2] T. Georgiou, R. Jalil, B. D. Belle, L. Britnell, R. V. Gorbachev, S. V. Morozov, Y.-J. Kim, A. Gholinia, S. J. Haigh, O. Makarovsky, L. Eaves, L. A. Ponomarenko, A. K. Geim, K. S. Novoselov, and A. Mishchenko, Nat. Nano **8**, 100 (2013).

[3] W. Zhang *et al.*, Sci. Rep. **4**, 3826 (2014).

[4] W. J. Yu, Y. Liu, H. Zhou, A. Yin, Z. Li, Y. Huang, and X. Duan, Nat. Nanotech. **8**, 952 (2013).

[5] H. Coy Diaz, R. Addou, and M. Batzill, Nanoscale **6**, 1071 (2014).

[6] D. Pierucci, H. Henck, C. H. Naylor, H. Sediri, E. Lhuillier, A. Balan, J. E. Rault, Y. J. Dappe, F. Bertran, P. Le Fèvre, A. T. C. Johnson, and A. Ouerghi, Sci. Rep. **6**, 26656 (2016).

[7] B. Sachs, L. Britnell, T. O. Wehling, A. Eckmann, R. Jalil, B. D. Belle, A. I. Lichtenstein, M. I. Katsnelson, and K. S. Novoselov, Appl. Phys. Lett. **103**, 251607 (2013).

[8] K.-G. Zhou, F. Withers, Y. Cao, S. Hu, G. Yu, and C. Casiraghi, ACS Nano **8**, 9914 (2014).

[9] Y. Gao, Q. Liu, and B. Xu, ACS Nano **10**, 5431 (2016).

[10] H. J. Conley, B. Wang, J. I. Ziegler, R. F. Haglund, S. T. Pantelides, and K. I. Bolotin, Nano Lett. **13**, 3626 (2013).

[11] H. Kumar, D. Er, L. Dong, J. Li, and V. B. Shenoy, Sci. Rep. **5**, 10872 (2015).

[12] Y. He, Y. Yang, Z. Zhang, Y. Gong, W. Zhou, Z. Hu, G. Ye, X. Zhang, E. Bianco, S. Lei, Z. Jin, X. Zou, Y. Yang, Y. Zhang, E. Xie, J. Lou, B. Yakobson, R. Vajtai, B. Li, and P. Ajayan, Nano Lett. **16**, 3314 (2016).

[13] Z. Liu, M. Amani, S. Najmaei, Q. Xu, X. Zou, W. Zhou, T. Yu, C. Qiu, A. G. Birdwell, F. J. Crowne, R. Vajtai, B. I. Yakobson, Z. Xia, M. Dubey, P. M. Ajayan, and J. Lou, Nat. Commun. **5**, 5246 (2014).

[14] L. Yang, X. Cui, J. Zhang, K. Wang, M. Shen, S. Zeng, S. A. Dayeh, L. Feng, and B. Xiang, Sci. Rep. **4**, 5649 (2014).

[15] A. Michail, N. Delikoukos, J. Parthenios, C. Galiotis, and K. Papagelis, Appl. Phys. Lett. **108**, 173102 (2016).

[16] J. E. Lee, G. Ahn, J. Shim, Y. S. Lee, and S. Ryu, Nat. Commun. **3**, 1024 (2012).

[17] C. Neumann, S. Reichardt, P. Venezuela, M. Drögeler, L. Banszerus, M. Schmitz, K. Watanabe, T. Taniguchi, F. Mauri, B. Beschoten, S. V. Rotkin, and C. Stampfer, Nat. Commun. **6**, 8429 (2015).

[18] A. Tiberj, M. Rubio-Roy, M. Paillet, J. R. Huntzinger, P. Landois, M. Mikolasek, S. Contreras, J. L. Sauvajol, E. Dujardin, and A. A. Zahab, Sci. Rep. **3**, 2355 (2013).

[19] T. G. A. Verhagen, K. Drogowska, M. Kalbac, and J. Vejpravova, Phys. Rev. B **92**, 125437 (2015).

[20] W. H. Chae, J. D. Cain, E. D. Hanson, A. A. Murthy, and V. P. Dravid, Appl. Phys. Lett. **111**, 143106 (2017).

[21] Y.-R. Lee, J.-X. Huang, J.-C. Lin, and J.-R. Lee, J. Phys. Chem. C **121**, 27427 (2017).

[22] T. Lee, F. A. Mas'ud, M. J. Kim, and H. Rho, Sci. Rep. **7**, 16681 (2017).

[23] F. Pizzocchero, L. Gammelgaard, B. S. Jessen, J. M. Caridad, L. Wang, J. Hone, P. Bøggild, and T. J. Booth, Nat. Commun. **7**, 11894 (2016).

[24] P. J. Zomer, M. H. D. Guimarães, J. C. Brant, N. Tombros and B. J. van Wees, Appl. Phys. Lett. **105**, 013101 (2014).

[25] D. M. Basko, S. Piscanec, and A. C. Ferrari, Phys. Rev. B **80**, 165413 (2009).

[26] S. Ryu, L. Liu, S. Berciaud, Y.-J. Yu, H. Liu, P. Kim, G. W. Flynn, and L. E. Brus, Nano Lett. **10**, 4944 (2010).

[27] K. Dolui, I. Rungger, and S. Sanvito, Phys. Rev. B **87**, 165402 (2013).

[28] D. Liu, Y. Guo, L. Fang, and J. Robertson, Appl. Phys. Lett. **103**, 183113 (2013).

[29] Z. Lin, B. R. Carvalho, E. Kahn, R. Lv, R. Rao, H. Terrones, M. A. Pimenta, and M. Terrones, 2D Mater. **3**, 022002 (2016).

[30] A. Das, S. Pisana, B. Chakraborty, S. Piscanec, S. Saha, U. Waghmare, K. Novoselov, H. Krishnamurthy, A. Geim, A. Ferrari, and A. Sood, Nat. Nanotech. **3**, 210 (2008).

[31] B. Chakraborty, A. Bera, D. V. S. Muthu, S. Bhowmick, U. V. Waghmare, and A. K. Sood, Phys. Rev. B **85**, 161403(R) (2012).

[32] S. Pisana, M. Lazzeri, C. Casiraghi, K. S. Novoselov, A. K. Geim, A. C. Ferrari, and F. Mauri, Nat. Mater. **6**, 198 (2007).

[33] A. Bera, D. V. S. Muthu, and A. K. Sood, J. Raman Spectrosc. **49**, 100 (2017).

[34] T. M. G. Mohiuddin, A. Lombardo, R. R. Nair, A. Bonetti, G. Savini, R. Jalil, N. Bonini, D. M. Basko, C. Galiotis, N. Marzari, K. S. Novoselov, A. K. Geim, and A. C. Ferrari, Phys. Rev. B **79**, 205433 (2009).

[35] Y. C. Cheng, Z. Y. Zhu, G. S. Huang, and U. Schwingenschlögl, Phys. Rev. B **83**, 115449 (2011).

[36] J. Zabel, R. R. Nair, A. Ott, T. Georgiou, A. K. Geim, K. S. Novoselov, and C. Casiraghi, Nano Lett. **12**, 617 (2012).

[37] J. E. Proctor, E. Gregoryanz, K. S. Novoselov, M. Lotya, J. N. Coleman, and M. P. Halsall, Phys. Rev. B **80**, 073408 (2009).

[38] C. Rice, R. J. Young, R. Zan, U. Bangert, D. Wolverson, T. Georgiou, R. Jalil, and K. S. Novoselov, Phys. Rev. B **87**, 081307(R) (2013).

[39] Y. Wang, C. Cong, C. Qiu, and T. Yu, Small **9**, 2857 (2013).

[40] C. Casiraghi, S. Pisana, K. S. Novoselov, A. K. Geim, and A. C. Ferrari, Appl. Phys. Lett. **91**, 233108 (2007).

[41] K. S. Novoselov, A. K. Geim, S. V. Morozov, and D. Jiang, Science **306**, 666 (2004).

[42] S. Berciaud, S. Ryu, L. E. Brus, and T. F. Heinz, Nano Lett. **9**, 346 (2009).

[43] R. Rao, G. Chen, L. M. R. Arava, K. Kalaga, M. Ishigami, T. F. Heinz, P. M. Ajayan, and A. R. Harutyunyan, Sci. Rep. **3**, 1891 (2013).

[44] C. C. Chen, W. Bao, J. Theiss, C. Dames, C. N. Lau, and S. B. Cronin, Nano Lett. **9**, 4172 (2009).

[45] S. Sahoo, A. P. S. Gaur, M. Ahmadi, M. J. F. Guinel, and R. S. Katiyar, J. Phys. Chem. C **117**, 9042 (2013).

[46] J.-U. Lee, K. Kim, and H. Cheong, 2D Mater. **2**, 044003 (2015).

[47] R. Yan, J. R. Simpson, S. Bertolazzi, J. Brivio, M. Watson, X. Wu, A. Kis, T. Luo, A. R. Hight Walker, and H. G. Xing, ACS Nano **8**, 986 (2014).

[48] D. Yoon, Y.-W. Son, and H. Cheong, Nano Lett. **11**, 3227 (2011).

[49] C. Sevik, Phys. Rev. B **89**, 035422 (2014).

[50] B. El-Kareh, *Fundamentals of Semiconductor Processing Technology* (Springer, Boston, MA, 2012).

[51] O. Frank, J. Vejpravova, V. Holy, L. Kavan, and M. Kalbac, Carbon **68**, 440 (2014).

[52] C.-J. Shih, Q. H. Wang, Y. Son, Z. Jin, D. Blankschtein, and M. S. Strano, ACS Nano **8**, 5790 (2014).

[53] H. Ago, H. Endo, P. Solis-Fernandez, R. Takizawa, Y. Ohta, Y. Fujita, K. Yamamoto, and M. Tsuji, ACS Appl. Mater. Interfaces **7**, 5265 (2015).

[54] L. Du, H. Yu, M. Liao, S. Wang, L. Xie, X. Lu, J. Zhu, N. Li, C. Shen, P. Chen, R. Yang, D. Shi, and G. Zhang, Appl. Phys. Lett. **111**, 263106 (2017).

[55] A. Splendiani, L. Sun, Y. Zhang, T. Li, J. Kim, C.-Y. Chim, G. Galli, and F. Wang, Nano Lett. **10**, 1271 (2010).

[56] K. F. Mak, C. Lee, J. Hone, J. Shan, and T. F. Heinz, Phys. Rev. Lett. **105**, 136805 (2010).

[57] K. F. Mak, K. He, C. Lee, G. H. Lee, J. Hone, T. F. Heinz, and J. Shan, Nat. Mater. **12**, 207 (2013).

[58] See Supplemental Material at http://link.aps.org/supplemental/10.1103/PhysRevB.99.195401 for optical characterization (PL and Raman maps) of Het-2.